Couplex Benchmark Computations with UG

Peter Bastian and Stefan Lang
Interdisciplinary Center for Scientific Computing, Universität Heidelberg, Im Neuenheimer Feld 368, 69120 Heidelberg, Germany

November 29, 2002

Abstract. This paper describes the numerical results for the COUPLEX benchmark obtained with the simulation software UG using vertex centered finite volume and higher order discontinuous Galerkin schemes. Multigrid solvers on unstructured grids, local mesh refinement and parallel computation are employed to yield very accurate solutions. Since the full range of results required in the benchmarks is too large to be displayed in this paper we focus on the comparison of discretization schemes, assessment of numerical errors and the presentation of parallel computations.

Keywords: flow, transport, finite volume scheme, discontinuous Galerkin scheme, parallel computation

1. Introduction

In 2001 ANDRA (agence nationale pour la gestion des déchets radioactifs) proposed a benchmark for porous medium flow and transport simulations in connection with the safety assessment of underground waste repositories in clay formations. The complete specification of the benchmark is given in [*this issue*]. This paper describes the results obtained with the simulation software UG [8] and the numerical methods that have been used. The focus of this work is on the comparison of discretization schemes, assessment of numerical errors through mesh refinement studies and the presentation of parallel computations. In order to be self-contained we shortly review the relevant model equations and the COUPLEX benchmark.

Let Ω be a domain in $\mathbb{R}^d$, $d = 2, 3$, with outward unit normal n. The equation for groundwater flow in head-based formulation is given by

$$\nabla \cdot u = f \qquad \text{in } \Omega, \quad u = -K\nabla H, \tag{1}$$

with Dirichlet boundary conditions $H = H_0$ on Γ_H and flux boundary conditions $u \cdot n = U$ on boundary Γ_U. H is the hydraulic head, u is the Darcy velocity and K is the permeability tensor.

The challenge for numerical methods solving (1) is to achieve high accuracy for the flow velocity u subsequently entering the transport equation. Moreover, the permeability tensor may vary over many orders of magnitude.

The generic mass balance equation including convective and dispersive transport as well as radioactive decay reads

$$R\omega\left(\frac{\partial C}{\partial t}+\lambda C\right)+\nabla\cdot j = q(C) \text{ in } \Omega, \quad j = uC - D(u)\nabla C \tag{2}$$

with Dirichlet boundary conditions $C = C_0$ on Γ_C, flux boundary conditions $j \cdot n = J$ on boundary Γ_J and outflow boundary conditions $j \cdot n = (uC - D(u)\nabla C) \cdot n$ on Γ_O. We assume that $u \cdot n \geq 0$ on Γ_O. R is the retardation factor, ω the effective porosity, $\lambda = \log 2/T$ with T the half life time of the element and D the diffusion/dispersion tensor.

The COUPLEX benchmark consists of three phases. COUPLEX 1 requires a far field simulation in a layered aquifer system of $25km \times 700m$. Nuclide transport is described by linear transport and decay (2) in a stationary flow field given by (1). The waste repository is modelled by a source term $q(x)$ located in a region of $3km \times 6m$. The difficulty of COUPLEX 1 lies in the anisotropic repository geometry combined with the large range of concentration values $C \in [10^{-12}, 10^{-2}]$ to be computed. Moreover, the permeability K varies by 7 orders of magnitude.

COUPLEX 2 requires a detailed three-dimensional simulation of a single elementary cell of the repository which is assumed to be repeated periodically. In total the transport of 10 components has to be computed which partly depend on each other through a nonlinear dissolution-precipitation term $q(C)$. Additionally, COUPLEX 2 requires the implementation of periodic boundary conditions which is non-trivial for unstructured mesh codes. COUPLEX 3 is an extension of COUPLEX 1 with the source term being the result of the COUPLEX 2 simulation.

Equation (1) is an elliptic equation for the hydraulic head H. Transport simulations require an accurate approximation of the velocity u in the presence of large permeability contrasts. Moreover, the computed flow field should be locally conservative. In this work we use the vertex centered finite volume scheme and the higher order discontinuous Galerkin method for the solution of the flow equation. The latter scheme is comparable in accuracy and efficiency with the mixed finite element method.

The transport equation (2) is hyperbolic for $D = 0$, otherwise it is parabolic. If D is small compared to u the equation is singularly perturbed. It is formally parabolic but may exhibit certain features of hyperbolic equations, e. g. solutions with sharp fronts.

Let us define the dimensionless numbers

$$Cr = |u|\Delta t/h \quad \text{and} \quad Pe = |u|h/D, \tag{3}$$

where we assumed that D is isotropic.

The Courant number Cr describes the propagation speed in terms of mesh cells and Pe measures the relative strength of convection and diffusion. If the mesh size h, velocity u and diffusion coefficient D vary spatially the Courant and Peclet numbers are defined locally.

State-of-the-art methods for solving instationary hyperbolic problems ($Pe = \infty$) are the high-resolution schemes such as the higher-order Godunov method, ENO-schemes [29] and the Runge-Kutta Discontinuous Galerkin method [19, 17, 21]. These schemes are constructed by combining a conservative spatial discretization with explicit TVD time-stepping schemes and slope or flux limiters. Limiters are necessary to remove unphysical oscillations from the numerical solution. In order to ensure stability, an upper bound on Cr is required. Implicit schemes are usually not used for transient hyperbolic problems because accuracy demands time steps similar in size to that of explicit schemes and unphysical oscillations are hard to avoid. High-resolution implicit schemes are possible but require the solution of nonlinear algebraic equations while having the same time-step restriction as explicit schemes [28]. Higher-order implicit schemes are efficient, however, if the solution is smooth and large time steps are required.

Efficient methods for the parabolic case $Pe = 0$ are constructed from spatial discretizations for elliptic problems combined with implicit temporal discretizations for stiff ordinary differential equations (method of lines approach). Since solutions tend to get smoother with time, large time-steps should be possible.

For problems with $0 < Pe < \infty$, many different methods have been proposed. For large Peclet numbers explicit methods are very efficient. One can show for standard schemes (second order Godunov with cell centered finite volumes) that $Cr < 1 < Pe$ allows the use of fully explicit schemes. The time step must be restricted to ensure stability but accuracy demands a time step of similar size. Methods of this type are presented in [22, 20, 1]. If $Pe < 1$ the fully implicit approach [34] is applicable because no sharp fronts are present in the solution. In the COUPLEX benchmark the Peclet number varies in space over several orders of magnitude. In that case operator splitting methods may be used which treat the convective part explicitly and the diffusive part implicitly. If the solution is smooth, as is the case in the COUPLEX benchmark, higher order implicit schemes are the method of choice. Moreover, the COUPLEX benchmark demands the computation of long time intervals with nearly stationary solution. This can only be done efficiently with implicit methods.

We note that there are alternative approaches to solve the transport equation based on the method of characteristics [23, 15, 3, 40]. These methods maintain sharp fronts while allowing large time-steps.

The paper is organized as follows. In Sections 2 and 3 we describe the vertex centered finite volume method and the higher order discontinuous Galerkin scheme. The PDE software framework UG underlying all the computations is described in Section 4 while Sections 5 and 6 contain the numerical results for COUPLEX 1 and COUPLEX 2, respectively. Conclusions are given in Section 7.

2. Vertex Centered Finite Volume Scheme

In this section we present the vertex centered finite volume (VCFV) scheme which has been widely used for computational fluid mechanics computations [38, 30, 13]. Combined with the fractional step θ time stepping procedure it is used for COUPLEX 1 as well as COUPLEX 2.

2.1. NOTATION

Let $E_h = \{e_1, \ldots, e_{n_h}\}$ be a non-degenerate quasi-uniform subdivision of Ω where $e \in E_h$ is a triangle or quadrilateral if $d = 2$ and e is a tetrahedron, pyramid, prism or hexahedron with planar faces if $d = 3$. Let h denote the maximum diameter of the elements in E_h. In E_h the intersection of two elements is either a vertex, an edge or a face (if $d = 3$). The domain covered by $e \in E_h$ is denoted by Ω_e and the outward unit normal to Ω_e is n_e.

Let $B_h = \{b_1, \ldots, b_{m_h}\}$ be a secondary subdivision of Ω constructed from E_h as follows: In two dimensions connect the barycenter of an element with the midpoints of the edges of the element. This construction is shown in Figure 1. In three dimensions the barycenter of an element is connected to edge midpoints and face barycenters. The boxes $b \in B_h$ are the polygonal regions associated with each vertex of the mesh. The domain covered by $b \in B_h$ is denoted by Ω_b. The position of the vertex associated with $b \in B_h$ is x_b. Note that if b is associated with a boundary vertex we have that $x \in \partial\Omega_b$, cf. v_j in Figure 1. The outward unit normal to Ω_b is denoted by n_b.

We define the internal skeleton

$$\Gamma_{int} = \{\gamma_{e,b,b'} \mid \gamma_{e,b,b'} = \Omega_e \cap \partial\Omega_b \cap \partial\Omega_{b'} \text{ for } e \in E_h,\ b, b' \in B_h\} \quad (4)$$

where $\gamma_{e,b,b'} \subseteq I\!R^{d-1}$ is the intersection of two boxes within an element. Correspondingly, the external skeleton is defined as

$$\Gamma_{ext} = \{\gamma_{e,b} \mid \gamma_{e,b} = \partial\Omega_e \cap \partial\Omega_b \cap \partial\Omega \text{ for } e \in E_h,\ b' \in B_h\}. \quad (5)$$

With each $\gamma_{e,b,b'} \in \Gamma_{int}$ we associate a unit normal n. The orientation can be selected arbitrarily. With any $\gamma_{e,b} \in \Gamma_{ext}$ we associate the unit normal n oriented outward to Ω.

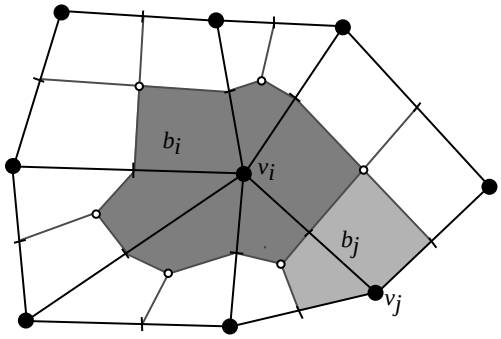

Figure 1. Construction of secondary mesh. Box b_i is associated with vertex v_i.

For any $x \in \gamma \in \Gamma_{int}$ we denote the jump of a function v by

$$[v](x) = \lim_{\epsilon \to 0+} v(x + \epsilon n) - \lim_{\epsilon \to 0+} v(x - \epsilon n). \tag{6}$$

Note that the jump is well defined for functions v being discontinuous on the skeleton Γ_{int}.

Finally we need the following finite element spaces.

$$V_h = \{v \in C^0(\Omega) \mid v \text{ is linear on } e \in E_h\} \tag{7}$$

is the standard conforming, piece-wise linear finite element space. Its subspace necessary for homogeneous Dirichlet boundary conditions is

$$V_{h0} = \{v \in V_h \mid v|_{\Gamma_H} = 0\}. \tag{8}$$

We also need the following discontinuous function space

$$W_h = \{w \in L^2(\Omega) \mid w \text{ is constant on } b \in B_h\} \tag{9}$$

and its subspace

$$W_{h0} = \{w \in W_h \mid w|_{\Gamma_H} = 0\}. \tag{10}$$

2.2. Scheme

The VCFV method can be written as a Petrov-Galerkin finite element method with continuous trial and discontinuous test functions.

Consider the case $H_0 = 0$ (homogeneous Dirichlet boundary conditions). Then the VCFV-scheme applied to the flow equation is defined as follows: Find $H \in V_{h0}$ such that for all $w \in W_{h0}$

$$-\sum_{\gamma \in \Gamma_{int}} \int_{\gamma} (K \nabla H) \cdot n[w] \, ds = \sum_{b \in B_h} \int_{\Omega_b} f w \, dx - \sum_{\gamma \in \Gamma_{ext} \cap \Gamma_U} \int_{\gamma} U w \, ds. \tag{11}$$

The case of inhomogeneous Dirichlet boundary conditions is treated as in the standard finite element method.

The VCFV-scheme applied to the transport equation is written in semi-discrete form. Again in the case of homogeneous Dirichlet boundary conditions $C_0 = 0$ the problem is to find $C(t) : [0,T] \to V_{h0}$ such that for all $w \in W_{h0}$ we have

$$\begin{aligned}
&\frac{\partial}{\partial t} \sum_{b \in B_h} \int_{\Omega_b} R\omega C w \; dx + \sum_{b \in B_h} \int_{\Omega_b} R\omega\lambda C w \; dx \\
&\quad + \sum_{\gamma \in \Gamma_{int}} \left\{ \int_\gamma C^* u \cdot n[w] \; ds - \int_\gamma (D\nabla C) \cdot n[w] \; ds \right\} \\
&\quad + \sum_{\gamma \in \Gamma_{ext} \cap \Gamma_O} \left\{ \int_\gamma C^* u \cdot n w \; ds - \int_\gamma (D\nabla C) \cdot n w \; ds \right\} \\
&= \sum_{b \in B_h} \int_{\Omega_b} q w \; dx - \sum_{\gamma \in \Gamma_{ext} \cap \Gamma_J} \int_\gamma J w \; ds.
\end{aligned} \tag{12}$$

The evaluation of C at $x \in \gamma_{e,b,b'}$ is denoted by C^* and is done as follows:

$$C^*(x) = (1-\beta)C(x) + \beta \begin{cases} C(x_b) & u \cdot n_b \geq 0 \\ C(x_{b'}) & u \cdot n_b < 0 \end{cases} . \tag{13}$$

The value $\beta = 1$ results in full upwinding and $\beta = 0$ corresponds to a second order formulation which is equivalent to central finite differences on certain meshes. The evaluation on the outflow boundary for $x \in \gamma_{e,b}$ is done in a similar way:

$$C^*(x) = (1-\beta)C(x) + \beta C(x_b). \tag{14}$$

The theoretical properties of the VCFV-scheme are treated extensively in [30, 13]. The spatial discretization error of the method in L^2 is first order if $\beta = 1$ and second order if $\beta = 0$ and the solution is sufficiently regular. Additional interesting properties of the method are:

- The method is locally conservative on the subdivision B_h.
- It is possible to treat full tensors D, which might be a problem in cell centered finite volume schemes.
- A discrete maximum princible (or, equivalently, stability in the maximum norm or M-matrix property of the stiffness matrix) can

be proven under certain restrictions: Discretization of the diffusion term leads to an M-matrix if the mesh is sufficiently regular. For triangular meshes the Delauney criterion is required (sum of two angles opposite an edge is at most π). The discretization of the convective term always leads to an M-matrix if $\beta = 1$ (upwind). In the case $\beta = 0$ one needs $Pe < 2$ and the Delauney criterion.

2.3. Fractional step θ scheme

Insertion of a basis for the function spaces V_{h0} and W_{h0} into Eq. (12) leads to a system of ordinary differential for the coefficients y_h which we denote in its generic form by

$$\frac{d}{dt} y_h = L_h(t, y_h(t)). \tag{15}$$

Here we describe certain implicit time discretizations used in connection with the VCFV-scheme.

The time interval $[0, T]$ is subdived into $0 = t^0 < t^1 < \ldots < t^M = T$ with $\Delta t^n = t^{n+1} - t^n$. The approximation of $y_h(t)$ to be computed is denoted by y_h^n.

The so-called one step θ scheme is given as follows:

$$y_h^{n+1} - \Delta t^n (1-\theta) L_h(t^{n+1}, y^{n+1}) = y_h^n + \Delta t^n \theta L_h(t^n, y^n) \tag{16}$$

Setting $\theta = 1$ gives the implicit Euler method and $\theta = 1/2$ corresponds to the Crank-Nicolson scheme. An improvement over these one step schemes is the fractional step θ scheme, which consists of three successive steps of the one step θ scheme with θ and Δt chosen in a special way:

$$\begin{array}{llll} \theta_1 = \sqrt{2} - 1 & \Delta t_1 = (\sqrt{2} - 1)\Delta t \\ \theta_2 = 2 - \sqrt{2} & \Delta t_2 = (1 - \sqrt{2}/2)\Delta t \\ \theta_3 = 2 - \sqrt{2} & \Delta t_3 = (1 - \sqrt{2}/2)\Delta t \end{array} \tag{17}$$

Each time step Δt is subdivided into the smaller time steps Δt_1, Δt_2 and Δt_3 but Δt is chosen three times as large as for the one step schemes. The fractional step scheme is 2nd order accurate and has improved stability properties (cf. [32]). The fractional step scheme is used in all VCFV computations for Couplex 1.

Within each substep a large system of linear algebraic equations has to be solved. This is done by so-called multigrid methods. Multigrid methods have the advantage of being of optimal, i. e . linear, complexity with respect to the number of unknowns. Standard references for multigrid methods are [25, 26]. Robust multigrid methods for porous medium applications are treated in [10, 16].

3. Discontinuous Galerkin Method

Due to their flexibility, discontinuous Galerkin (DG) methods have been popular among the finite element community and they have been applied to a wide range of computational fluid problems. Since the first DG method introduced in [33] the methods have been developed for hyperbolic problems known as the Runge-Kutta DG method [17, 21] and for elliptic problems in [41, 31, 20, 36, 37]. A unified analysis for many DG methods for elliptic problems has been given recently in [4]. A general overview is available in [18].

Advantages of DG methods are their higher order convergence property, local conservation of mass and flexibility with respect to meshing and *hp*-adaptive refinement. Their uniform applicability to hyperbolic, elliptic and parabolic problems as well as their robustness with respect to strongly discontinuous coefficients renders them very attractive for porous medium flow and transport calculations [35, 1]. DG methods for elliptic problems are comparable in quality with mixed finite element methods [5].

In this work we use a formulation due to Oden, Babuška, and Baumann [31] and combine it with diagonally implicit Runge-Kutta time discretizations.

3.1. Notation

Let E_h denote a subdivision of the domain Ω as defined above. The space of polynomial functions of degree r on element $e \in E_h$ is defined by

$$P_r(\Omega_e) = \{w : \Omega_e \to I\!R \mid w(x,y) = \sum_{0 \le a+b \le r} c_{ab}\ x^a y^b\}. \tag{18}$$

The extension to three space dimensions is obvious. Note that P_r can be used on triangles (tetrahedra) *and* quadrilaterals (hexahedra). In the implementation P_r is generated from basis polynomials on the reference element. Moreover, we use basis polynomials that are L^2-orthogonal on the reference elements. This improves the conditioning of the arising matrices and leads to diagonal mass matrices.
The finite element space used in the DG method is defined as

$$V^r(E_h) = \prod_{e \in E_h} P_r(\Omega_e). \tag{19}$$

Note that functions in $V^r(E_h)$ are discontinuous at element boundaries.

The skeleton Γ_{int} has to be redefined suitably to cope with the discontinuities at element boundaries. We define the internal skeleton

$$\Gamma_{int} = \{\gamma_{e,f} \mid \gamma_{e,f} = \partial\Omega_e \cap \partial\Omega_f\ \forall e, f \in E_h\}. \tag{20}$$

Correspondingly, the external skeleton is defined as

$$\Gamma_{ext} = \{\gamma_e \mid \gamma_e = \partial\Omega_e \cap \partial\Omega \ \forall e \in E_h\}. \tag{21}$$

With each $\gamma_{e,f} \in \Gamma_{int}$ we associate a unit normal n. The orientation can be selected arbitrarily. With any $\gamma_e \in \Gamma_{ext}$ we associate the unit normal n oriented outward to Ω.

In addition to the jump (6) we also define the average of a function at $x \in \gamma \in \Gamma_{int}$:

$$\langle v \rangle(x) = \frac{1}{2}\left(\lim_{\varepsilon \to 0+} v(x + \varepsilon n) + \lim_{\varepsilon \to 0+} v(x - \varepsilon n)\right). \tag{22}$$

3.2. Scheme

The DG scheme for solving the elliptic problem (1) is given as follows: Find $H \in V^r(E_h)$ such that for all $v \in V^r(E_h)$

$$\begin{aligned}
&\sum_{e \in E_h} \int_{\Omega_e} (K\nabla H) \cdot \nabla v \; dx \\
&\qquad + \sum_{\gamma \in \Gamma_{int}} \int_{\gamma} \langle K\nabla v \cdot n \rangle \, [H] - [v] \, \langle K\nabla H \cdot n \rangle \, ds \\
&\qquad + \sum_{\gamma \in \Gamma_{ext} \cap \Gamma_H} \int_{\gamma} (K\nabla v \cdot n) H - v \; K\nabla H \cdot n \; ds \\
&= \sum_{e \in E_h} \int_{\Omega_e} f v \; dx - \sum_{\gamma \in \Gamma_{ext} \cap \Gamma_U} \int_{\gamma} U v \; ds \\
&\quad + \sum_{\gamma \in \Gamma_{ext} \cap \Gamma_H} \int_{\gamma} (K\nabla v \cdot n) H_0 \; ds
\end{aligned} \tag{23}$$

Note that the Dirichlet boundary condition is approximated weakly. Assuming that the solution is sufficiently regular the convergence rate of the scheme in the energy norm (and thus for the velocity $u = -K\nabla H$) is $O(h^r)$ and the convergence rate in L^2 is $O(h^r)$ if r is even and $O(h^{r+1})$ if r is odd. This anomaly can can be remedied with other stabilizations such as the nonsymmetric interior penalty DG method or the local DG method [20, 37, 4].

Insertion of a basis into (23) results into a large system of linear equations. In [11] we developed an optimal order multigrid algorithm for solving these systems. It uses polynomials of the same degree r on the coarse grid and a point-block ILU smoother combined with a reordering strategy.

The local conservation property of the DG scheme becomes obvious when a test function $v \in V^r(E_h)$ with $v|_{\Omega_e} = 1$ is inserted. Then the scheme reduces to

$$\sum_{\gamma\in\Gamma_{int}} \int_\gamma [v]\ \langle u\cdot n\rangle ds + \sum_{\gamma\in\partial\Omega} \int_\gamma u\cdot n\ v\ ds = \sum_{e\in E_h} \int_{\Omega_e} fv\ dx \tag{24}$$

which shows that the conserved flux is the average $\langle u\cdot n\rangle$.

The Darcy velocity $u^{\mathrm{DG}} = -K\nabla H$ is discontinuous at element boundaries and does not have continuous normal component $u^{\mathrm{DG}}\cdot n$. Thus, the average flux $\langle u\cdot n\rangle$ is inconsistent with the fluxes evaluated from left and right. Mathematically we have $u^{\mathrm{DG}} \notin H(\mathrm{div};\Omega)$. A velocity field with continuous normal component is, however, required by most transport simulations such as the scheme described below. In [12] we describe a simple projection scheme $\Pi : (V^r(E_h))^d \to H(\mathrm{div};\Omega)$ and prove that the projection does not reduce the accuracy of the DG scheme. This projected velocity $u^* = \Pi(u^{\mathrm{DG}})$ is used in the transport simulation.

The semi-discrete DG scheme for solving problem (2) in either the hyperbolic or parabolic form is given as follows: Find $C : [0,T] \to V^r(E_h)$ such that for all $v \in V^r(E_h)$

$$\begin{aligned}
&\frac{\partial}{\partial t}\sum_{e\in E_h}\int_{\Omega_e} R\omega C v\ dx + \sum_{e\in E_h}\int_{\Omega_e} R\omega\lambda C v\ dx \\
&\quad - \sum_{e\in E_h}\int_{\Omega_e} (uC - D\nabla C)\cdot\nabla v\ dx + \sum_{\gamma\in\Gamma_{int}}\int_\gamma [v]C^*\langle u\cdot n\rangle\ ds \\
&\quad + \sum_{\gamma\in\Gamma_{int}}\int_\gamma \langle D\nabla v\cdot n\rangle[C] - [v]\langle D\nabla C\cdot n\rangle\ ds \\
&\quad + \sum_{\gamma\in\Gamma_{ext}\cap\Gamma_C}\int_\gamma (D\nabla v\cdot n)C - v(D\nabla C\cdot n)\ ds \\
&\quad + \sum_{\gamma\in\Gamma_{ext}\cap\Gamma^*}\int_\gamma vCu\cdot n\ ds \\
&= \sum_{e\in E_h}\int_{\Omega_e} qv\ dx - \sum_{\gamma\in\Gamma_{ext}\cap\Gamma_J}\int_\gamma Jv\ ds \\
&\quad - \sum_{\gamma\in\Gamma_{ext}\cap\Gamma'}\int_\gamma vC_0 u\cdot n\ ds + \sum_{\gamma\in\Gamma_{ext}\cap\Gamma_C}\int_\gamma D\nabla v\cdot n\ C_0\ ds
\end{aligned}$$

where we have used the refined decomposition of the boundary into outflow combined with Dirichlet outflow

$$\Gamma^* = \Gamma_O \cup \{x\in\Gamma_C \mid u(x)\cdot n > 0\} \tag{25}$$

and Dirichlet inflow

$$\Gamma' = \{x \in \Gamma_C \mid u(x) \cdot n \leq 0\}. \tag{26}$$

The concentration in the convective term for $x \in \gamma \in \Gamma_{int}$ is upwinded via

$$C^*(x) = \begin{cases} \lim\limits_{\epsilon \to 0+} C(x - \epsilon n) & \text{if } \langle u \cdot n \rangle \geq 0 \\ \lim\limits_{\epsilon \to 0+} C(x + \epsilon n) & \text{else} \end{cases} . \tag{27}$$

The spatial error of this formulation is $O(h^{r+1})$ in L^2 in the hyperbolic case ($D = 0$) for a sufficiently regular solution. Error estimates are provided in [34].

3.3. Diagonally Implicit Runge-Kutta Methods

After introducing a basis and inverting the mass matrix the scheme (25) can be written as a large system of ordinary differential equations (15) for the coefficients $y_h(t)$.

All Runge-Kutta methods used here can be written in the following form which computes y_h^{n+1} from a given y_h^n:

1. $y_h^{(i)} = \sum\limits_{k=1}^{i} \left[y_h^n + b_{ik} \Delta t^n L_h(t^n + d_k \Delta t^n, y_h^{(k)}) \right] \quad i = 1(1)s$;
2. $y_h^{n+1} = y_h^{(s)}$;

The number of stages of the scheme is s. For hyperbolic and convection-dominated parabolic problems explicit schemes with the total variation diminishing (TVD) property were developed in [39, 19]. In this work we use three diagonally *implicit* Runge-Kutta schemes with favourable stability characteristics: The strongly S-stable schemes of order 2 (with 2 stages) and 3 (with 3 stages) given in [2] and the L-stable scheme of order 4 with 5 stages which is given in [27].

No slope limiters are used in this scheme. We assume that the grid Peclet number is large enough to avoid oscillations. Within each stage of the Runge-Kutta method a large system of algebraic equations has to be solved. This is done with the Newton-Multigrid techniques.

4. PDE Simulation Software UG

The schemes described above have all been implemented on the basis of the software system UG [8, 6]. UG is an ongoing long-term development effort and establishes a software framework for the computation of partial differential equations (PDEs).

The following features are provided by the framework in a problem-independent and reusable way:

- Mesh management: Unstructured meshes in two and three space dimensions with six different element types as well as flexible placement of degrees of freedom.

- Parallelism: All modules realized inside UG provide their functionality also in parallel. Using parallel resources is nearly transparent on user level. Even an inexperienced user is able to use a powerful supercomputer to speed up his computations significantly by factors exceeding 10^2. As target platform to run the UG software the most scalable machine architecture is selected. Data exchange between processes (communication) is done via message passing, e.g. using MPI. The parallelization of UG is based on the flexible, graph-based programming model DDD [14, 7] which also supports dynamic migration of complex data structures.

- h-adaptivity: local grid adaption can be performed to concentrate the unknowns on areas where interesting phaenomena are expected or high accuracy of the solution is needed, e.g. the container region in the COUPLEX 2 benchmark.

- Multigrid methods: As solvers for the large linear systems multigrid methods are applied. Especially when performing parallel large-scale computations with millions of unknowns optimal complexity solvers are a key issue for scalability.

Over the last years, besides the couplex module, several other application modules in the context of subsurface flow have been realized. d^3f [24] is a simulator for density driven flow scenarios. Primarily it was designed to study flow phenomena in geological formations around salt domes. These salt domes play a central role in german nuclear waste repository management. The simulator includes tools to perform several stages of a case study: Modelling geological layers, grid generation, the numerical simulator and postprocessing tools for visualization. For transport simulation in fractured porous media a specialized module including fracture and grid generation has been developed, see [9]. Multiphase/multicomponent flow applications are described in [10, 16].

Key UG capabilities used in the COUPLEX benchmark are:

- Anisotropic mesh support: Bisection refinement rules can be applied to decrease geometric anisotropy. This capablity has been used in COUPLEX 2, to keep both element angles good and mesh anisotropy low.

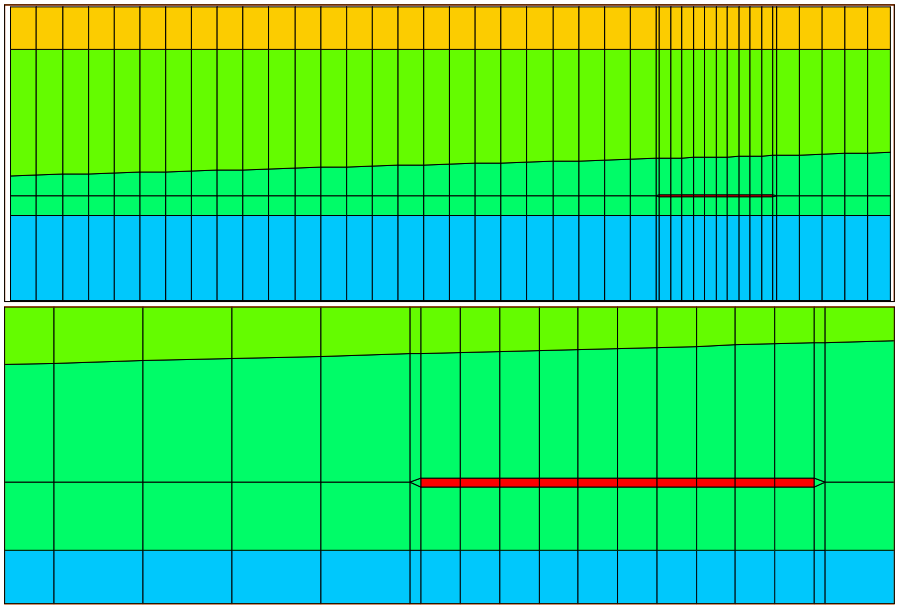

Figure 2. Initial coarse mesh for COUPLEX 1 simulation with zoom of the vicinity of the repository. Both plots are scaled by a factor 12 in y-direction.

– Periodic boundaries: An arbitrary number of periodic boundaries can be defined. These are transparent for local grid adaption and parallelism.

5. Couplex 1

5.1. MESHING

Figure 2 shows the coarse mesh with 222 elements used to discretize the COUPLEX 1 domain. In order to ensure a maximum principle obtuse angles had to be avoided. The anisotropic repository region is discretized with long and flat rectangular elements, then triangular elements are used to make the transition from the small side with a length of $6m$ to large elements needed in the rest of the domain. Structured mesh codes would result in a mesh with anisotropic elements also outside the repository region. To our knowledge no automatic mesh generator is able to produce a mesh comparable in quality to the hand-made one.

5.2. Grid Convergence of Transport Calculation

An important question in a nuclear waste management simulation is to determine the concentration levels at various positions in space and time. In this subsection we consider the concentration levels of ^{129}I at $t = 200000yr$ and try to assess the accuracy in the position of the isoline for concentration 10^{-8}. In order to do this we compute the concentration field with decreasing spatial and temporal mesh size. In particular we use 14521 (level 3), 56832 (level 4), 227328 (level 5) and 909312 (level 6) elements with, respectively, 52, 68, 68 and 104 timesteps. The result for the VCFV scheme using second order approximation for the convective terms ("central differences") is shown in Figure 3. The results do not show unphysical oscillations if the mesh is sufficently fine (level 4). This is a consequence of both: Small mesh Peclet number and good mesh design. As can be seen in Figure 3, the position of the isoline at the border between the clay and limestone layers is overestimated in the coarse grid simulation. With subsequent refinement the position of the contour line moves to the right.

The size of the time steps is varied from $100[yr]$ initially up to $10^5[yr]$ for the VCFV/fractional step scheme and $10^6[yr]$ for the DG/SDIRK schemes according to a prescribed schedule. Note that each time step is subdivided into three substeps in the fractional step and the SDIRK(3) scheme.

Let x_l be the position of the contour line computed with the second order VCFV scheme on level l which is shown in the first column of Table 5.2. From that data we estimate the convergence rate as

$$\frac{|x_6 - x_5|}{|x_5 - x_4|} \approx \frac{1}{3.5} \tag{28}$$

(where we expected an asymptotic convergence factor of 1/4) and therefore get the error estimate

$$|x_6 - x_{exact}| \leq \frac{|x_6 - x_5|}{3.5} \left(\frac{1}{1 - 1/3.5} \right) = 161 \ [m]. \tag{29}$$

Columns two, three and four of Table 5.2 contain the error estimates obtained with all three schemes schemes considered. The DG(2) scheme is formally second order accurate and yields an accuracy comparable to the second order VCFV scheme with about the same number of degrees of freedom (DOF). The error in the VCFV full upwind scheme is about 12 times larger than for the second order schemes for the same number of DOF.

A comparison of computation times is shown in Table 5.2. The DG scheme is significantly more efficient than the VCFV scheme mainly

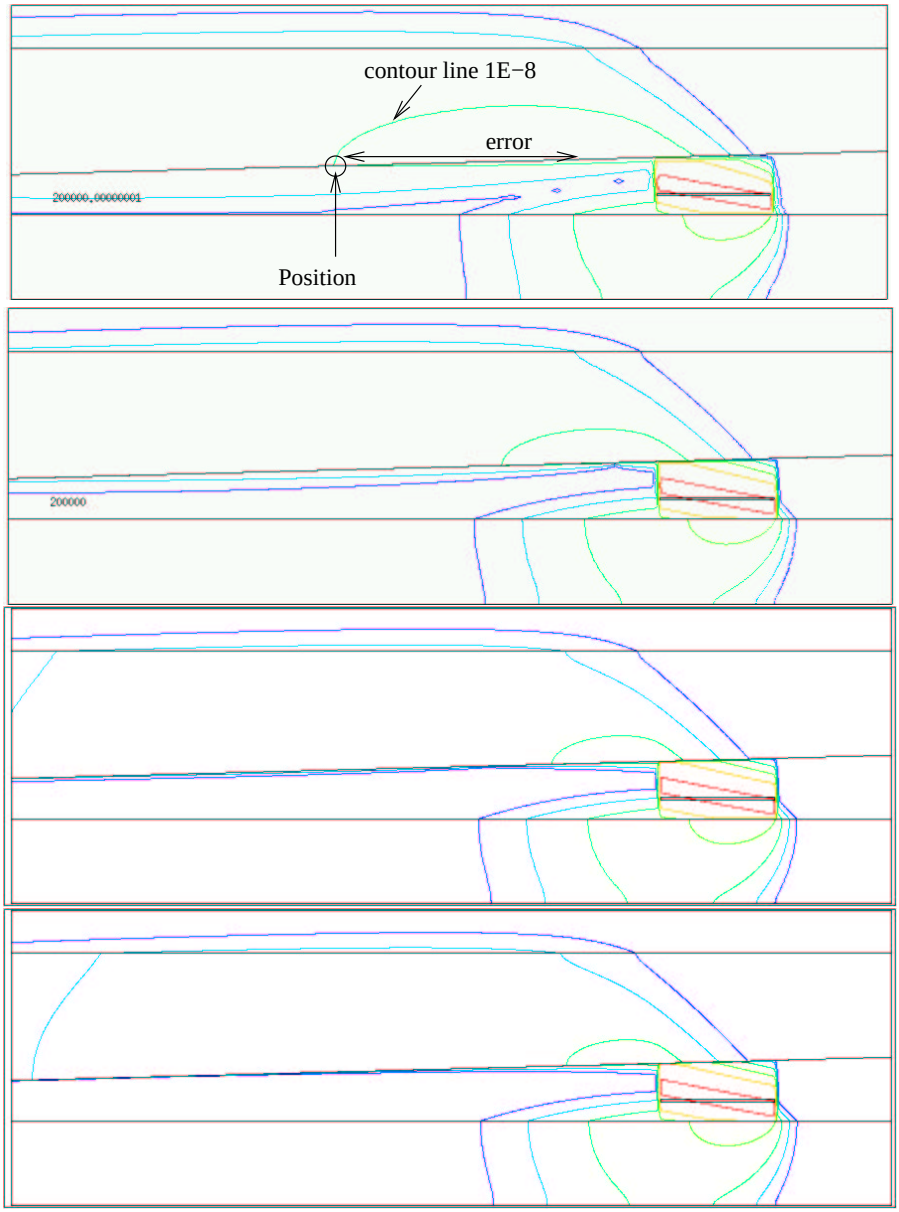

Figure 3. Contour lines of ^{129}I at $t = 200000yr$ computed with 2nd order VCFV/fractional step scheme on levels 3, 4, 5, 6 and 52, 68, 68 and 104 (FS-θ) time steps (from top). Colors code the contour lines: 10^{-12} (blue), 10^{-10} (light blue), 10^{-8} (light green), 10^{-6} (green), 10^{-4} (orange), 10^{-2} (red).

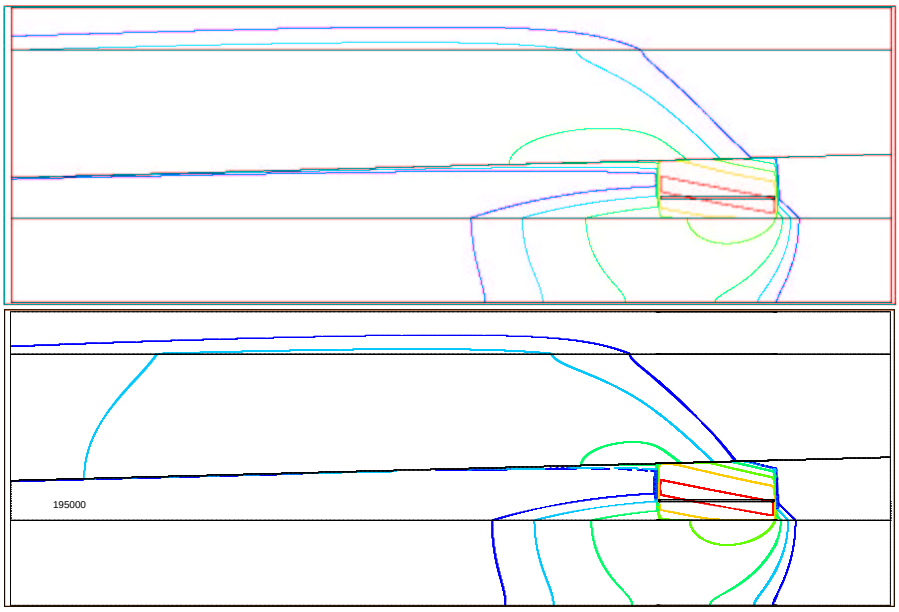

Figure 4. Contour lines of ^{129}I at $t = 200000yr$. Computed with full upwinding VCFV scheme on level 6 (top) and DG(2) in space, third order RK scheme in time on level 5 (bottom). Colors code the contour lines: 10^{-12} (blue), 10^{-10} (light blue), 10^{-8} (light green), 10^{-6} (green), 10^{-4} (orange), 10^{-2} (red).

Table I. Error analysis for x-position of the isoline 10^{-8} on the border of clay and limestone layer obtained with different discretization schemes and mesh refinements.

level	VCFV 2nd order/FS-θ		DG(2)/SDIRK(3)	VCFV full upwind/FS-θ
	position $[m]$	error $[m]$	error $[m]$	error $[m]$
3	15743	6760	-1240	17160
4	11089	1160	-540	7260
5	9604	560	-140	3860
6	9208	161	-	1860

because much larger time steps can be taken. The size of the time step is limited in the second order VCFV scheme because the linear systems get very difficult to solve due to loss of diagonal dominance.

5.3. Breakthrough Curves at Aquifer Boundary

Figure 5 shows the breakthrough curves for ^{129}I at the outflow boundary of the limestone layer obtained on meshes with 3725 up to 227809

Table II. Computation time for most accurate Couplex 1 calculations.

Scheme	DOF	time steps	processors	comp. time [h]
2nd Order VCFV	$0.9 \cdot 10^6$	1692	40 × PII/400	46.3
DG(2)/SDIRK(3)	$1.35 \cdot 10^6$	87	1 × PIV/2200	63.1

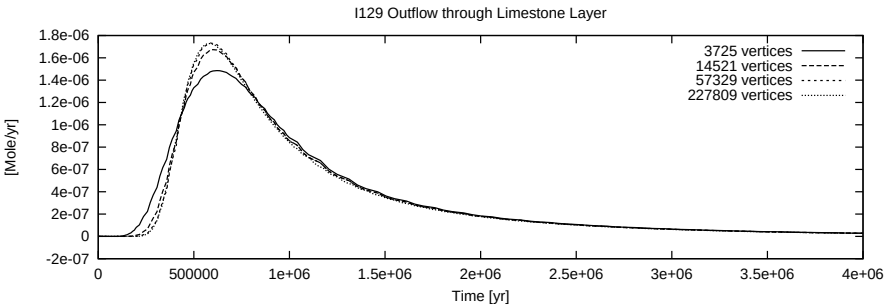

Figure 5. Breakthrough curves for ^{129}I at outflow boundary of limestone layers on successively refined meshes.

vertices. The figure shows that such an integral quantity can already be computed accurately on a relatively coarse mesh. The solutions obtained on the two finest meshes are almost undistinguishable.

6. Couplex 2

6.1. Global Solution Algorithm and Meshing

Couplex 2 involves the solution of in total 10 coupled equations for the dissolved components in the water phase: C_s (silica), C_0 (^{135}Cs), C_1 (^{238}Pu), C_{-1} (^{234}U), C_2 (^{242}Pu), C_{-2} (^{238}U) and the precipitated components in the solid phase: F_1 (^{238}Pu), F_{-1} (^{234}U), F_2 (^{242}Pu), F_{-2} (^{238}U). These equations are discretized with the 2nd order VCFV scheme in space and implicit Euler in time. The discrete equations for the coupled system are solved sequentially in blocks as follows: First the linear equation for C_s is solved, then that for C_0, then block $\{C_1, C_2, F_1, F_2\}$ and finally $\{C_{-1}, C_{-2}, F_{-1}, F_{-2}\}$ are solved in a fully coupled way using Newton-Multigrid because these unknowns are non-linearly dependent on each other through the precipitation term.

The domain used in the Couplex 2 computation is $18 \times 24.8 \times 100[m^3]$ and contains exactly one container (i. e. we use half of the

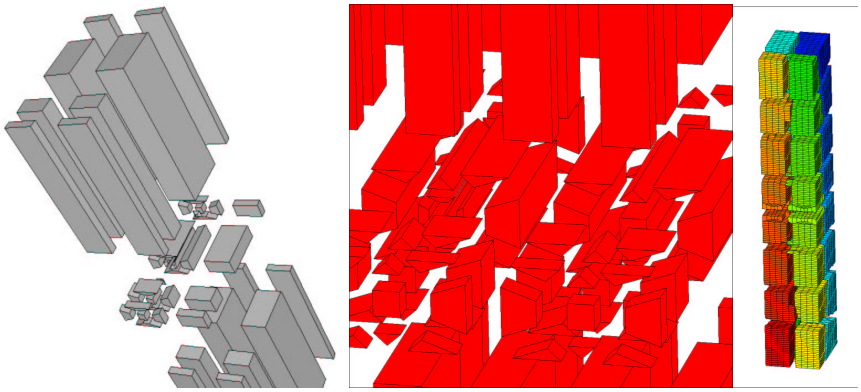

Figure 6. Minimal mesh to resolve geometry (left), final inital mesh, which is conforming across periodic boundaries (middle), mesh with element anisotropy reduced by directed refinement and load balancing of mesh onto processors (right).

domain proposed in the benchmark document due to symmetry). The meshing of the COUPLEX 2 geometry with its components backfill, seal, buffer and container was done manually to avoid bad angles. The resulting unstructured triangulation involves hexahedra and prisms. The left picture in figure 6 shows the minimal triangulation to resolve the geometry. Across periodic boundaries the mesh has to match. This requirement leads to the final triangulation, which is visualized in figure 6 in the middle picture. The starting mesh is then further refined using directed refinement. Bisection rules for prisms/hexahedra and trisection rules for hexahedra were realized to reduce element anisotropy and furthermore improve element angles. The directed bisection of prisms introduces two new elements: a prism and a hexahedron with angles equal or better than the angles of the refined prism. This is done until element anisotropies are better than 1/2.5 and element angles do not exceed 135 degrees. This initial refinement phase to improve mesh quality resulted in a mesh with 1182 elements and 1622 vertices. After further uniform refinement and load balancing onto 32 processors the mesh looks like in the right picture of figure 6.

Figure 7 shows the isosurfaces of the Cesium concentration at three different times computed on a mesh with 79862 vertices.

6.2. COMMENTS ON GLASS DISOLUTION MODEL

The COUPLEX benchmark document proposes a detailed model of glass dissolution in Section 3.3 resulting in a Fourier type boundary condition

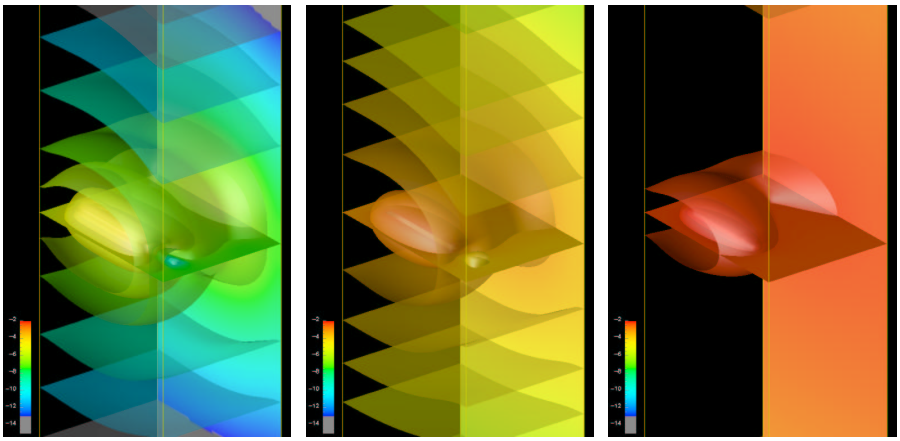

Figure 7. Concentration isosurfaces of Cesium after 10^4, 10^5 and 10^6 years.

at the container. The equation for silica transport is given by

$$\phi R_s \frac{\partial C_s}{\partial t} + \nabla \cdot j_s(C_s) = \frac{\rho_p \nu_p}{\lambda_p} \left(1 - \frac{C_s}{S_p}\right) \text{ in } \Omega \tag{30}$$

where the (sligthly modified) boundary condition at the container is given by

$$j_s(C_s) \cdot n = -\rho_m \nu_m \left(1 - \frac{C_s}{S_m}\right). \tag{31}$$

Note that the two equilibrium concentrations $S_p = 0.54$ $[mol/m^3]$ and $S_m = 0.82$ $[mol/m^3]$ are different. This results in a boundary layer which is hard to resolve numerically. The size of the boundary layer depends on the various constants given in the equation above. Unfortunately, the parameter λ_p is not specified uniquely but is allowed to range from $8 \cdot 10^{-10}$ to 10^{-3} which, consequently, leads to a large variation in the size of the boundary layer. In this section we compute the size of the boundary layer analytically under the assumption that the convective/dispersive fluxes in Eq. (30) can be neglected. Then we will verify the analytical observations by highly resolved computations.

Let B be a cube of size h^3 located with one face at the container boundary. Integration of (30) over B gives

$$\phi R_s \frac{\partial}{\partial t} \int_B C_s dx + \int_{\partial B} j_s(C_s) \cdot n \; ds = \int_B \frac{\rho_p \nu_p}{\lambda_p} \left(1 - \frac{C_s}{S_p}\right) dx. \tag{32}$$

Neglecting convective/diffusive fluxes over interior boundaries, inserting the boundary condition and assuming C_s to be constant in B

results in an ordinary differential equation

$$\phi R_s h^3 \frac{\partial C_s}{\partial t} - \rho_m \nu_m \left(1 - \frac{C_s}{S_m}\right) h^2 = h^3 \frac{\rho_p \nu_p}{\lambda_p} \left(1 - \frac{C_s}{S_p}\right), \tag{33}$$

which, after some algebraic manipulation, can be written in the form

$$\phi R_s \frac{\partial C_s}{\partial t} = \left(\frac{\rho_p \nu_p}{\lambda_p} + \frac{\rho_m \nu_m}{h}\right) \left(1 - \frac{C_s}{S^*}\right) \tag{34}$$

with

$$S^*(\lambda_p, h) = \frac{S_p S_m \left(\frac{\rho_p \nu_p}{\lambda_p} + \frac{\rho_m \nu_m}{h}\right)}{\frac{\rho_p \nu_p}{\lambda_p} S_m + \frac{\rho_m \nu_m}{h} S_p}. \tag{35}$$

S^* is the value of C_s for $t \to \infty$ at the container boundary computed by a numerical scheme (say VCFV) on a mesh of size h under the assumption that convective/dispersive fluxes can be neglected. It can be shown that S^* is achieved very quickly with respect to the time scale of COUPLEX 2 (i. e. after a few years).

Note that $S^*(\lambda_p, h)$ is still a function of λ_p and h since both parameters can be chosen by the implementor of COUPLEX 2. Figure 8 shows the dependence of S^* on the mesh size for the given range of λ_p and directly visualizes the boundary layer. Note that h is given on a logarithmic scale. According to Figure 8 it requires a mesh resolution of $h = 10^{-6}$ $[m]$ for $\lambda_p = 10^{-6}$ in order to resolve the boundary layer!

This consideration has direct consequences for the dissolution time (time where all the silica in the container has been dissolved). Since S^* converges to S_m for $h \to 0$ the flux in the boundary condition (31) converges to 0 and consequently the dissolution time is ∞.

Taking convective/dispersive fluxes into account will result in a limiting value below S_m at the container boundary. This effect can only be analysed by numerical computations on meshes which are highly resolved in the vicinity of the container. Table 6.2 shows the corresponding results for a local mesh size as small as $1.25 \cdot 10^{-2}[m]$ obtained through local mesh refinement. Clearly, the boundary layer can be resolved for $\lambda_p = 10^{-3}$ and the concentration at the container boundary converges to a value ≈ 0.747. For smaller values of λ_p the boundary layer cannot be resolved due to mesh size limitations but the effect can be seen.

The fact that the silica concentration at the container boundary is highly sensitive to both mesh size h and parameter λ_p renders this model unsuitable for a benchmark computation. The validity of this model should be checked carefully. For these reasons we decided to use the flux boundary condition with $\tau = 10^{-2}$ for our COUPLEX 2 computations.

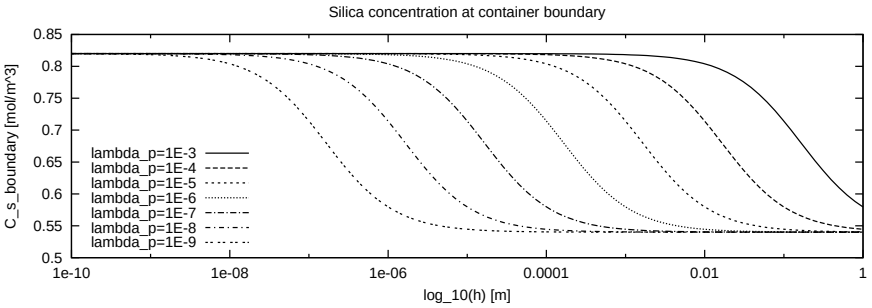

Figure 8. Silica concentration at container boundary depending on λ_p and mesh size h.

Table III. Computed concentration value of silica at container boundary $x = 4.95$, $y = 13.33$, $z = 50$ after $t = 250[yr]$ for various mesh sizes and values of parameter λ_p.

$h[m]$	λ_p			
	10^{-3}	10^{-4}	10^{-5}	10^{-6}
0.4	0.6496	0.5574	0.5418	0.5402
0.2	0.6976	0.5754	0.5441	0.5404
0.1	0.7287	0.6034	0.5484	0.5409
0.05	0.7416	0.6356	0.5564	0.5418
0.025	0.7455	0.6586	0.5695	0.5436
0.0125	0.7464	0.6683	0.5851	0.5469

6.3. Convergence of Breakthrough Curves

As one result of the Couplex 2 computation we consider the breakthrough curves for the dissolved components C_0 (^{135}Cs) and C_{-1} (^{234}U) at the upper and lower domain boundaries (host to outside) in more detail. These two components have been chosen since C_0 is governed by a linear equation and C_{-1} is governed by a nonlinear equation (precipitation). Moreover, these results are the input of the Couplex 3 computation and therefore have direct influence on the accuracy of the far field computation.

Figure 9 shows the corresponding breakthrough curves. Clearly the results for ^{135}Cs can be obtained quite accurately already on a very coarse mesh. However, the accurate computation of the breakthrough curve for ^{234}U requires a much finer mesh. To reduce the relative error in

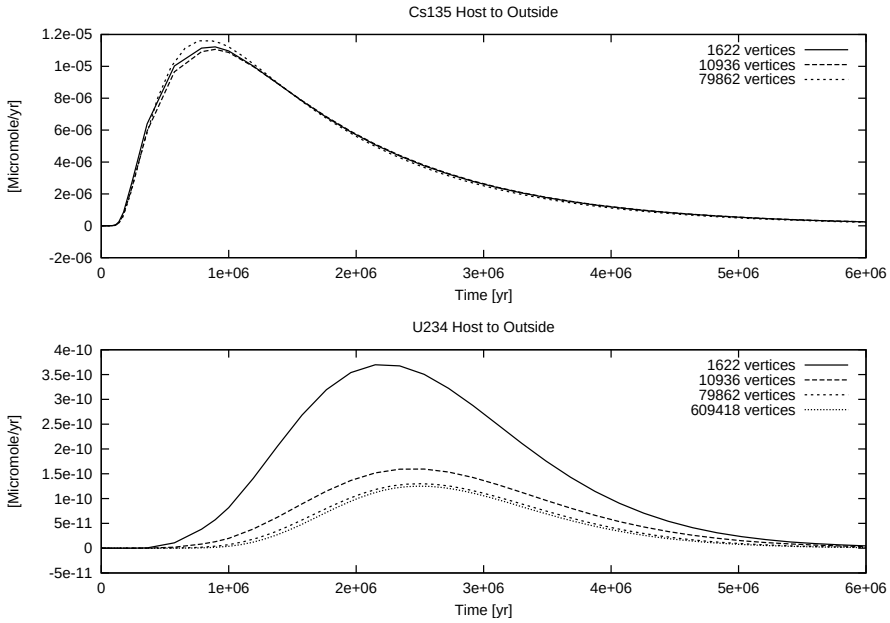

Figure 9. Breakthrough curves for ^{135}Cs (top) and ^{234}U (bottom) at upper and lower boundaries of the domain.

the peak value to about 1% requires the calculation on 609418 vertices with 6703598 degrees of freedom.

6.4. Parallel Computation

Total execution time for three different Couplex 2 configurations are listed in Table 6.4. Computations have been performed on the HELICS cluster consisting of AMD Athlon 1.3 GHz processors connected by a Myrinet 2000 interconnect. In the configurations the problem size is roughly scaled with the number of processors. All computation times (reported in seconds) are in the range of a few hours. It can be seen that the largest computation on more than $6 \cdot 10^6$ degrees of freedom would require 9 days computing time on a sequential machine using 6 GB main memory! Above, it has been demonstrated that grid convergence for the ^{234}U breakthrough curve is obtained only with this fine mesh computation. Therefore, parallelization was absolutely necessary for a successful computation of the Couplex 2 benchmark. Table 6.4 also contains the time needed per time step and the resulting speedup per time step.

Table IV. Parallel Speedup of COUPLEX 2 computations with 1, 8 and 64 Timesteps. To increase accuracy also in time dimension timestep sizes have been varied.

P	DOF	Timesteps	Job time [s]	Time/Step [s]	Speedup/Step
1	120296	50	8621	172	-
8	878482	57	22720	398	3.5
64	6703598	74	23040	311	35.4

7. Conclusions

In this paper we demonstrate that a successful computation of the COUPLEX benchmark is an interdisciplinary task that requires knowledge about the underlying partial differential equations, accurate discretization schemes, efficient solvers and simulator software that is providing support for unstructured meshes, local refinement and parallel computation. We have shown that estimates of the error in the unknown solution can be obtained through systematic mesh refinement studies which is extremely important in repository safety analysis. This assessment of numerical errors required computations on about 10^7 degrees of freedom in three space dimensions over long time intervals which can only be done effectively with high-performance computing capabilites.

Acknowledgements

We greatly acknowledge the use of the "HEidelberg LInux Cluster System" for the parallel computations.

References

1. Aizinger, V., C. Dawson, B. Cockburn, and P. Castillo: 2001, 'The local discontinuous Galerkin method for contaminant transport'. *Adv. Wat. Res.* **24**, 73–87.
2. Alexander, R.: 1977, 'Diagonally implicit Runge-Kutta methods for stiff O.D.E.'s'. *SIAM Journal Numer. Anal.* **14**, 1006–1021.
3. Arbogast, T. and M. F. Wheeler: 1995, 'A characteristics-mixed finite element method for advection-dominated transport problems'. *SIAM J. Numer. Anal.* **32**, 404–424.
4. Arnold, D., F. Brezzi, B. Cockburn, and L. Marini: 2002, 'Unified analysis of discontinuous Galerkin methods for elliptic problems'. *SIAM J. Numer. Anal.* **39**(5), 1749–1779.

5. Bastian, P.: 2003, *Numerical Computation of Multiphase Flows*. Springer-Verlag. in preparation.
6. Bastian, P., K. Birken, K. Johannsen, S. Lang, N. Neuss, H. Rentz-Reichert, and C. Wieners: 1998, 'Parallel Unstructured Grid Computations'. In: W. Hackbusch (ed.): *Proceedings of the* 14^{th} *GAMM Seminar Kiel*. .
7. Bastian, P., K. Birken, and S. Lang: 1999, 'High level software tools for unstructured adaptive grids on massively parallel systems'. In: *Proc. of 9th SIAM Conf. on Parallel Processing for Scientific Computing*. p. published on CD.
8. Bastian, P., K. Birken, S. Lang, K. Johannsen, N. Neuß, H. Rentz-Reichert, and C. Wieners: 1997, 'UG: A flexible software toolbox for solving partial differential equations'. *Computing and Visualization in Science* **1**, 27–40. , .
9. Bastian, P., Z. Chen, R. Ewing, R. Helmig, H. Jakobs, and V. Reichenberger: 2000, 'Numerical Solution of Multiphase flow in Fractured porous media'. In: Z. Chen, R. Ewing, and Z. Shi (eds.): *Numerical treatment of multiphase flows in porous media*. pp. 50–68.
10. Bastian, P. and R. Helmig: 1999, 'Efficient fully-coupled solution techniques for two-phase flow in porous media. Parallel multigrid solution and large scale computations'. *Adv. Water Res.* **23**, 199–216. .
11. Bastian, P. and V. Reichenberger: 2000, 'Multigrid for higher order discontinuous Galerkin finite elements applied to groundwater flow'. Technical Report 2000-37, SFB 359. .
12. Bastian, P. and B. Rivière: 2002, 'Superconvergence and H(div)-projection for discontinuous Galerkin methods'. Technical Report 2002-23, IWR, Universität Heidelberg. , submitted to Int. J. Numer. Meth. Fluids.
13. Bey, J.: 1998, *Finite–Volumen– und Mehrgitterverfahren für elliptische Randwertprobleme*, Advances in Numerical Mathematics. Stuttgart: Teubner-Verlag.
14. Birken, K.: 1998, 'Ein Modell zur effizienten Parallelisierung von Algorithmen auf komplexen, dynamischen Datenstrukturen'. Ph.D. thesis, Universität Stuttgart.
15. Celia, M., T. Russel, I. Herrera, and R. Ewing: 1990, 'An Eulerian–Lagrangian localized adjoint method for the advection–diffusion equation'. *Adv. Water Resources* **13(4)**, 187–206.
16. Class, H., R. Helmig, and P. Bastian: 2002, 'Numerical simulation of non-isothermal multiphase multicomponent processes in porous media. 1. An efficient solution technique'. *Adv. Wat. Res.* **25**, 533–550. .
17. Cockburn, B., S. Hou, and C. Shu: 1990, 'TVB Runge-Kutta local projection discontinuous Galerkin finite element method for conservation laws IV: The multidimensional case'. *Math. Comput.* **54**, 545.
18. Cockburn, B., S. Lin, and C. Shu (eds.): 2000, 'Discontinuous Galerkin methods. Theory, computation and applications', Vol. 11 of *Lecture Notes in Computational Science and Engineering*. Springer-Verlag.
19. Cockburn, B. and C. Shu: 1991, 'The Runge-Kutta local projection P^1-discontinuous Galerkin method for scalar conservation laws'. M^2 *AN* **25**, 337.
20. Cockburn, B. and C. Shu: 1998a, 'The local discontinuous Galerkin finite element method for convection-diffusion systems'. *SIAM J. Numer. Anal.* **35**, 2440–2463.
21. Cockburn, B. and C. Shu: 1998b, 'The Runge-Kutta discontinuous Galerkin method for conservation laws V: Multidimensional systems'. *J. Comput. Phys.* **141**, 199–224.

22. Dawson, C.: 1991, 'Godunov–mixed methods for advective flow problems in one space dimension'. *SIAM J. Numer. Anal.* **28(5)**, 1282–1309.
23. Douglas Jr., J. and T. Russel: 1982, 'Numerical Methods for convection dominated diffusion problems based on combining the method of characteristics with finite element or finite difference procedures'. *SIAM J. Numer. Anal.* **19(5)**, 871–885.
24. Fein, E. (ed.): 1998, 'd^{3}f – Ein Programmpaket zur Modellierung von Dichteströmungen'. GRS-139.
25. Hackbusch, W.: 1985, *Multi–Grid Methods and Applications*. Springer–Verlag.
26. Hackbusch, W.: 1994, *Iterative Solution of Large Sparse Systems of Linear Equations*. Springer.
27. Hairer, E. and G. Wanner: 1991, *Solving ordinary differential equations II*. Springer, Berlin.
28. Harten, A. and P. Lax: 1984, 'On a class of high-resolution total-variation-stable finite-difference schemes'. *SIAM J. Numer. Anal.* **21**, 1–23.
29. LeVeque, R.: 1992, *Numerical Methods for Conservation Laws*. Birkhäuser.
30. Michev, I.: 1996, 'Finite volume and finite volume element methods for nonsymmetric problems'. Ph.D. thesis, Texas A&M University.
31. Oden, J., I. Babuška, and C. Baumann: 1998, 'A Discontinuous *hp* Finite Element Method for Diffusion Problems'. *Journal of Computational Physics* **146**, 491–519.
32. Rannacher, R.: 1994, 'Accurate Time Discretization Schemes for Computing Nonstationary Incompressible Fluid Flow'. In: *Proceedings of the International Conference on Computational Methods in Water Resources X*. pp. 1239–1246.
33. Reed, W. and T. Hill: 1973, 'Triangular mesh methods for the neutron transport equation'. Technical report, Los Alamos Scientific Laboratory.
34. Rivière, B. and M. Wheeler: 2002, 'Nonconforming methods for transport with nonlinear reaction'. In: Z. Chen and R. Ewing (eds.): *Fluid Flow and Transport in Porous Media: Mathematical and Numerical*, Vol. 295. American Mathematical Society, pp. 421–432.
35. Rivière, B., M. Wheeler, and K. Banaś: 2000, 'Part II. Discontinuous Galerkin method applied to a single phase flow in porous media'. *Comput. Geosci.* **4**, 337–349.
36. Rivière, B., M. Wheeler, and V. Girault: 1999, 'Improved energy estimates for interior penalty, constrained and discontinuous Galerkin methods for elliptic problems I'. *Comput. Geosci.* **3**, 337–360.
37. Rivière, B., M. Wheeler, and V. Girault: 2001, 'A priori error estimates for finite element emthods based on discontinuous approximation spaces for elliptic problem'. *SIAM Journal on Numerical Analysis* **39**(3), 902–931.
38. Schneider, G. and M. Raw: 1986, 'A Skewed, Positive Influence Coefficient Upwinding Procedure for Control-Volume-Based Finite-Element Convection-Diffusion Computation'. *Numerical Heat Transfer* **9**, 1–26.
39. Shu, C.: 1988, 'Total-variation-diminishing time discretizations'. *SIAM J. Sci. Stat. Comput.* **9**(6), 1073–1084.
40. Wang, H., H. Dahle, R. Ewing, M. Espedal, R. Sharpley, and S. Man: 1999, 'An ELLAM scheme dor advection-diffusion equations in two dimensions'. *SIAM J. Sci. Stat. Comput.* **20**(6), 2160–2194.
41. Wheeler, M.: 1978, 'An elliptic collocation finite element method with interior penalties'. *SIAM J. Numer. Anal.* **15**(1), 152–161.